International Journal of Heat and Mass Transfer 160 (2020) 120166

Contents lists available at ScienceDirect

International Journal of Heat and Mass Transfer

journal homepage: www.elsevier.com/locate/hmt

Sliding on ice: Real contact area, melted film thickness, and friction force

Changho Yun[a,1], Jin Woo Choi[a,1], Hyungseok Kim[a,b,1], Dongjo Kim[a], Ho-Young Kim[a,*]

[a] Department of Mechanical Engineering, Seoul National University, Seoul 08826, Korea
[b] Department of Mechanical Engineering, Massachusetts Institute of Technology, 77 Massachusetts Avenue, Cambridge, MA 02139, USA

ARTICLE INFO

Article history:
Received 21 February 2020
Revised 20 June 2020
Accepted 2 July 2020

Keywords:
Ice
Friction
Melting
Liquid film
Contact area
Visualization

ABSTRACT

It is easy to slide on ice because of water films arising as a consequence of frictional melting. Although the friction force of ice and a slider critically depends on the area and thickness of the liquid film as well as the sliding speed, direct experimental visualization and quantification of temporal evolutions of the contact area, film thickness, and the resulting friction force have been scarce to date. Here we develop an experimental technique to visualize the contact area of ice asperities and a high-speed sliding surface in situ based on the optical principle of total internal reflection. We construct a hydrodynamic model to predict the contact area, liquid film thickness and friction force of a model system of hemispherical ice on a flat solid surface. Upon showing good agreement between theory and experiment, we briefly discuss how the fundamental understanding of the friction behavior of a single ice bump can be extended to understand the friction behavior of flat ice surfaces.

1. Introduction

Why it is so easy to slide on ice has aroused scientific interests over a century [1–3], and it is now widely accepted that a water film arising from frictional melting lowers the dynamic friction coefficient [4,5]. However, predicting the actual friction coefficient of a high-speed macroscopic slider on ice is by no means easy because the melted liquid film is formed only at the real contact area of the slider with ice and its thickness is unknown *a priori*. Unlike common materials like polymers and metals that exist as solids at room temperature, ice is most often prepared by freezing water under various conditions and thus its surface condition is extremely hard to control and characterize [6,7]. The naturally present surface roughness leads to localized melting of ice where randomly distributed protrusions of the two surfaces of ice and slider touch. The friction forces caused by viscous shear of the melted regions depend on the temporal evolution of the ice-slider contact area and the liquid film thickness.

To go beyond the observation of the static contact area between a specimen and ice [8,9], the contacting surface was previously examined through measuring the worn-off area of ice after friction test via the scanning electron microscopy [10,11], the X-ray computer tomography [10], the optical microscopy [12], and the white light interferometry [13]. Although those studies revealed that protrusions of ice surface are flattened because of melting by frictional heat, the in situ observation of the ice-slider contact area has rarely been achieved except for a report for a low sliding speed (< 1 m s^{-1}) [14]. Here, we employ an optical setup based on the principle of total internal reflection. Although such technique was previously used to observe the contact areas of polymer-glass [15–18] and metal-glass [19], we apply the technique to the ice-slider contact for the first time to our knowledge. In addition to the contact area, we simultaneously measure the friction force in situ, which allows us to understand dynamic friction behavior of ice from the hydrodynamics of the melted lubricating film.

Because we are concerned with the temporal evolution of contact area caused by melting of ice during sliding, we theoretically consider the transport rates of heat and mass associated with melting, squeezing and translation of the liquid film. Thus, our model is distinguished from previous theoretical studies for the friction of ice and slider with a constant contact area [20–22]. Our analytical model leads to scaling laws for the contact area, liquid film thickness and the friction force as functions of time and pertinent physical parameters (such as density, viscosity, and geometry and velocity of a slider), which facilitate experimental verification of our theory. If the liquid film thickness and the consequent friction force are precisely quantified and theoretically modeled based on clearly visualized temporal evolutions of the contact area, one can better understand and control the ice friction arising in a va-

* Corresponding author.
E-mail address: hyk@snu.ac.kr (H.-Y. Kim).
[1] These authors contributed equally to this work.

https://doi.org/10.1016/j.ijheatmasstransfer.2020.120166
0017-9310/

riety of settings including winter sport games [23–25], transportations [24,26], glacier movements [22,24,27], and snow avalanche [24,28].

We are focused on the conditions where the melting of ice plays an important role in friction, or the ambient temperature is not far from the melting point of ice. It is because the situation would be little different from other normal solid contacts if the friction occurs at temperature considerably lower than the melting point. Therefore, the tribological regime considered here belongs to either mixed or hydrodynamic friction. However, the lubricant liquid layer in our experiments is a direct outcome of the melting of the participant solid (ice), rather than being externally applied.

We note that quasi-liquid layers (QLL) can be present on the surface of ice at the temperature not far from the melting point [29,30]. Although the properties of QLL were reported for a stationary ice surface [31–33] and at the sliding onset of ice against silica surfaces [34], the presence of QLL on ice surfaces sliding at such a high speed as investigated in this work has not been confirmed to date. Thus, we preclude the effects of QLL in our results.

In the following, we describe an experimental technique to visualize in situ the real contact area between ice and a slider while simultaneously measuring the friction force. We then construct a hydrodynamic theory to predict the contact area, melted film thickness, and the consequent friction force as a function of the materials properties, solid geometry, sliding velocity and time. We first use a hemispherical ice specimen and a flat slider as a model system, which allows us to observe and measure the contact behavior of a single contact spot. We then briefly discuss how such fundamental theory can be used to understand the friction between flat ice and slider.

2. Experimental

Fig. 1 shows the experimental apparatus to visualize the contact area and measure the friction force between ice and quartz. Using a rotational stage of 300 mm in diameter, we obtain the linear sliding speed at the circumference ranging from 1 to 10 m s^{-1}. We use two different shapes of ice in the experiments – hemisphere (Fig. 1(a)) and flat plate (Fig. 1(c)). The hemispheres model individual asperities of real flat surfaces. Furthermore, the hemispherical ice ensures a single contact area with the rubbing surface, and thus allows for repeatable experimental data and reliable theoretical modeling. Similar approaches were previously employed to obtain repeatable friction coefficient data with ice hemispheres on flat rubber surfaces [11] and with spherical rubber specimens on flat ice surfaces [9]. In Fig. 1(a), the flat quartz disk rotates while the ice is stationary. In Fig. 1(c), the ice ring rotates while the quartz prism is held still. In both the experiments, the real contact area and the friction force are obtained simultaneously with a high-speed camera (Photron Fastcam Mini UX50) and a load cell (HBM PW4C3/300g), respectively. The polished quartz surface has the root mean square roughness of approximately 200 nm as measured by the atomic force microscope (Park Systems XE-70). All the experiments are carried out in a chamber where the temperature is maintained constant with the relative humidity kept at approximately 20%.

Fig. 1 (b) illustrates the optical principle used to image the contact area between hemispherical ice and the quartz surface. The light leaving the source arrives at the high-speed camera via total internal reflection at the quartz-air interface, while the light penetrates the quartz-ice interface, when the incident angle θ satisfies $n_a/n_q < \sin\theta < n_w/n_q$. Here, n is the refractive index and the subscripts a, q and w designate air, quartz and water, respectively: $n_a = 1.00$, $n_q = 1.46$ and $n_w = 1.33$. The area where melted ice (water) and the quartz are in real contact are imaged dark surrounded by the bright non-contact region. Fig. 1(d) illustrates similar beam trajectories to visualize the contact area of flat but randomly rough ice and quartz surfaces.

Great care is needed to prepare ice specimens without air bubbles and distortion, which is essential to obtain reliable data in the visualization and measurements of contact area and friction force. We cooled water in a container from below to help trapped air escape through the water surface exposed to the atmosphere, and to accommodate volume expansion during freezing by letting water brim over the container. For a hemispherical ice specimen, we cooled deionized water in a hollow hemispherical mold of poly(dimethylsiloxane) (PDMS) coated with hydrophobic poly(tetrafluoroethylene) (PTFE), as shown in Fig. 1(e). To obtain a flat ice surface, we cooled water contained in a circular track of aluminum with the upper face down, as shown in Fig. 1(f). The temperature of the thermoelectric cooler was maintained at -10°C during freezing while the entire apparatus was housed in a chamber of constant temperature and humidity with the interior air temperature of 5 $^{\circ}$C. After the water was fully frozen, the thermoelectric cooler was turned off and ice was thermally equilibrated to the surrounding air temperature, -0.5°C.

Fig. 2 shows the experimentally aquired images of the temporal evolutions of the contact areas between quartz and ice. When the hemispherical ice contacts a sliding quartz disk, a circular contact area grows with time as shown in Fig. 2(a). Unlike the contact of hemispheres with a flat surface, the seemingly flat ice plate contacts the quartz prism only partially through limited number of contact spots, as shown in Fig. 2(b). The number and area of contact spots varies with time while their locations appear to move to the left following the rotating ice. Theoretical considerations of those contact areas, film thickness and the resultant friction force are given in the following.

3. Theoretical analysis

3.1. Friction of an ice hemisphere

Since the friction of two surfaces is a result of collective interactions at individual contact spots, it is fundamental to understand the temporal evolution of the single contact area as shown in Fig. 2(a). For theoretical modeling of the contact area of hemispherical ice and a flat slider, we consider a water film with thickness h and area A as shown in Fig. 3. We find h and A by balancing the rates of heat generation due to viscous dissipation and the rate of heat absorbed by ice to melt into water.

The viscous dissipation at the water film generates heat, which is either consumed to melt ice or transferred to the environments by conduction. The heat for ice melting per unit area, q_m, is given by $q_m = \rho_i L\dot{H}$ where $\dot{H} = \mathrm{d}H/\mathrm{d}t$ is the rate of change of ice height due to melting, and ρ_i and L is the density and the latent heat of ice, respectively. The conduction heat transfer rate per unit area, $q_{c,j}$, to the ice ($j = i$) and the quartz specimen ($j = s$) is scaled as $q_{c,j} \sim k_j(T_m - T_\infty)/\delta_j$, where k_j is the thermal conductivity, T_m is the melting temperature of ice, and T_∞ is the far-field temperature. We scale the thickness of the thermal boundary layer, δ_j, as $\delta_j \sim \sqrt{\alpha_j \tau_j}$ with α_j and τ_j respectively being the thermal diffusivity and the duration of contact. We write $\tau_i = t$, where t is the duration of the sliding experiment as the ice hemisphere continually encounters the quartz specimen. But any point in the quartz specimen meets the ice only for $\tau_s \sim d/U$, where d is the diameter of the contact area and U is the sliding velocity. We can show that the conductive heat loss is negligible compared with the latent heat, or $q_{c,j}/q_m \ll 1$, with $j = i$ or $j = s$, because $T_m - T_\infty \ll \rho_i L\dot{H}\sqrt{\alpha_j \tau_j}/k_j$ in our experimental conditions.

Assuming the two-dimensional Couette flow inside the water film, the viscous dissipation per unit area consists of that occurring in the bulk, $q_v \sim \mu U^2/h$ with μ being the viscosity of water, and

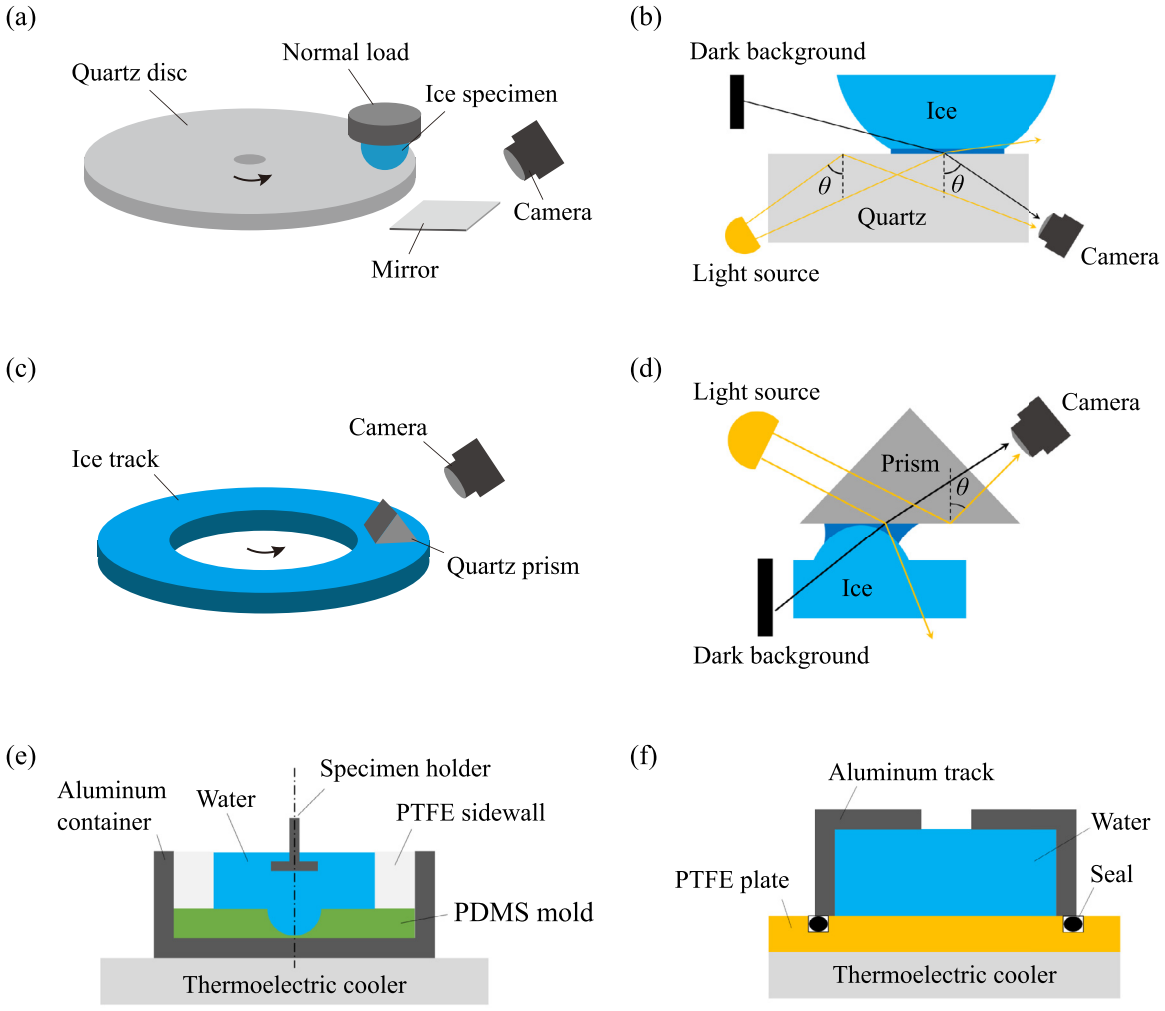

Fig. 1. Experimental apparatus to visualize the contact area and measure the friction force between ice and a solid surface with a high relative velocity. (a) Friction test between a hemispherical ice specimen and a rotating quartz disk. (b) Principle of contact area visualization using total internal reflection of light at the quartz-air interface. (c) Friction test between the quartz prism and a rotating ice track. (d) Principle of contact area visualization using total internal reflection of light at the quartz-air interface. (e) A schematic of the setup to prepare a hemispherical ice specimen, which is to be removed from the mold with the specimen holder after freezing. (f) A schematic of the setup to prepare a flat ice specimen in a circular track, which is to be used in the friction test after turned upside down.

that occurring near the contact line, Φ. We estimate $\Phi \sim \mu\Gamma U^2/d$, where $\Gamma = \ln(\Lambda/\lambda)$ with Λ being the length scale of the wedge and λ the cutoff length of molecular scale [35,36]. The cutoff length is introduced to prevent the integration of the viscous dissipation function over the wedge volume near the contact line from blowing up. For $d \gg \Gamma h$ in our experimental conditions with Γ typically ranging from 1 to 10, we get $q_v \gg \Phi$.

Now balancing the melting heat, q_m, with the viscous heat generation, q_v, gives

$$\dot{H} \sim \frac{\mu U^2}{\rho_i L h}. \tag{1}$$

A geometric consideration for the shape of the truncated hemisphere of initial radius R in Fig. 3 allows us to relate A and H as

$$A = \pi H(2R - H). \tag{2}$$

We need one more equation to close the system to obtain three unknowns, A, h and H, as a function of time, which comes from the mass conservation. The rate of change of the film, $\dot{\Omega}$, is due to the influx of liquid by melting of ice, $\dot{\Omega}_m$, the outflux of liquid caused by squeezing of normal load, $\dot{\Omega}_s$, and the outflux of liquid owing to the relative translation of the plate, $\dot{\Omega}_t \sim UhA^{1/2}$: $\dot{\Omega} = \dot{\Omega}_m - \dot{\Omega}_s - \dot{\Omega}_t$. With the water density denoted as ρ_w, we write $\dot{\Omega}_m = (\rho_i/\rho_w)\dot{H}A$. The squeezed flow rate from a disk under a normal load of F_n, without considering the relative translation of the bottom plate, is given by $\dot{\Omega}_s = 2\pi F_n h^3/(3\mu A)$ assuming the inertia-free flow. The volume conservation is simplified to $\dot{\Omega}_m \approx \dot{\Omega}_t$ under the following assumptions. First, the normal load is weak enough to satisfy $\dot{\Omega}_s \ll \dot{\Omega}_m$. Second, the rate of film expansion is low as compared with $\dot{\Omega}_m$ and $\dot{\Omega}_t$. Then we obtain

$$\dot{H} \sim \frac{\rho_w}{\rho_i} UhA^{-1/2}. \tag{3}$$

Now we seek scaling relations for A, H and h after simplifying Eq. (2) to $A \approx 2\pi RH$ assuming that $H \ll 2R$, which holds for a significant duration of the melting. Combining relations (1) and (3) gives the following power laws:

$$A \sim \rho_w^{2/5}\rho_i^{-4/5}\mu^{2/5}L^{-2/5}U^{6/5}R^{4/5}t^{4/5}, \tag{4}$$

$$H \sim \rho_w^{2/5}\rho_i^{-4/5}\mu^{2/5}L^{-2/5}U^{6/5}R^{-1/5}t^{4/5}, \tag{5}$$

$$h \sim \rho_w^{-2/5}\rho_i^{-1/5}\mu^{3/5}L^{-3/5}U^{4/5}R^{1/5}t^{1/5}. \tag{6}$$

We compare the scaling law for A with our measurement result of the contact area between the quartz plate and the ice hemisphere of different radii, sliding velocities and downward normal

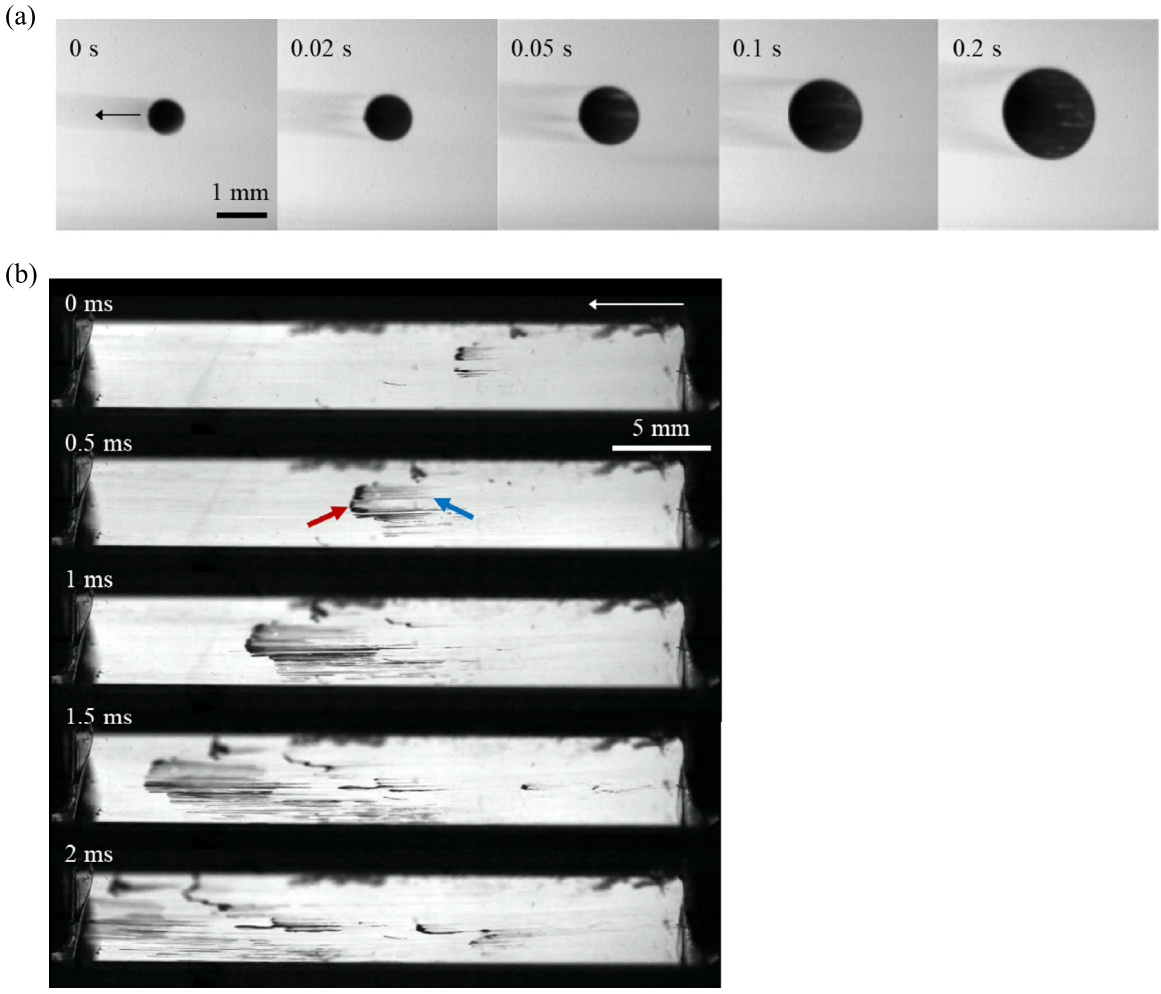

Fig. 2. (a) Temporal evolution of the dark contact area of an ice hemisphere of radius 3 mm with a quartz disk moving at a velocity of 3.2 m s^{-1}. The temperature is −0.5°C and the normal load is 1.45 N. The black arrow indicates the sliding direction of the rotating quartz with respect to the stationary ice. (b) Temporal evolution of dark contact area of a quartz prism (30 × 10 mm^2 in area) with ice disc with the relative velocity of 10 m s^{-1}. The temperature is −0.5°C and the normal load is 2.7 N. The white arrow indicates the sliding direction of the rotating ice with respect to the stationary quartz prism. The red and blue arrows respectively indicate a front and tail of a contact area. (For interpretation of the references to color in this figure legend, the reader is referred to the web version of this article.)

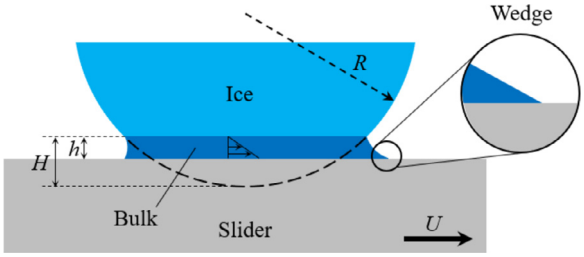

Fig. 3. The schematic of a liquid film and the velocity profile at the contact area of ice and slider. H is measured from the lowest point of the original ice hemisphere to the top of liquid film.

forces, in Fig. 4. The scattered raw data of A for different experimental conditions in Fig. 4(a) are collapsed onto a single line in Fig. 4(d), consistent with our theory. We obtain the best fitting straight line until A equals R^2 to satisfy our geometric assumption $H \ll 2R$. With the empirically determined prefactor in Fig. 4(d), $k_A = 3.21$, we write $A \approx k_A \rho_w^{2/5} \rho_i^{-4/5} \mu^{2/5} L^{-2/5} U^{6/5} R^{4/5} t^{4/5}$ and $H \approx k_A (2\pi)^{-1} \rho_w^{2/5} \rho_i^{-4/5} \mu^{2/5} L^{-2/5} U^{6/5} R^{-1/5} t^{4/5}$ until the experimental data deviate from the theoretical straight line in the late stages. The deviation begins when H is no longer negligible compared with $2R$ in Eq. (2). Therefore, the foregoing scaling laws, (4)–(6), are strictly valid when $A \ll 4\pi R^2$ or $t \ll (4\pi/k_A)^{5/4} \rho_w^{-1/2} \rho_i \mu^{-1/2} L^{1/2} U^{-3/2} R^{3/2}$.

In the scaling laws, we see that A, H and h all increase with U and t, corresponding to the enhanced melting of ice. However, the loss of ice in the longitudinal direction, H, decreases, unlike A and h, as the original size of the hemisphere, R increases. It is because the longitudinal melting rate, $\dot{H}$, is decreased with the increase of A as shown in relation (3).

Because the friction comes from the hydrodynamic viscous force arising at the liquid film of thickness h, we write the friction force $F \approx \mu UA/h$, which gives the scaling law for F:

$$F \sim \rho_w^{4/5} \rho_i^{-3/5} \mu^{4/5} L^{1/5} U^{7/5} R^{3/5} t^{3/5}. \quad (7)$$

Fig. 4 (b) shows the experimentally measured values of the friction force that scatter for different experimental conditions. But they tend to be collapsed onto a single line when plotted according to relation (7) in Fig. 4(e) except for deviation in the late stages with the increase of $H/(2R)$ to a level no longer negligible compared with unity.

While the simple morphology of the hemispherical ice gives H directly from A, the precise value of film thickness h, whose scaling law is given in Eq. (6), can be deduced by combining the measurement results of A and the friction force F: $h \approx \mu UA/F$. Fig. 4(c)

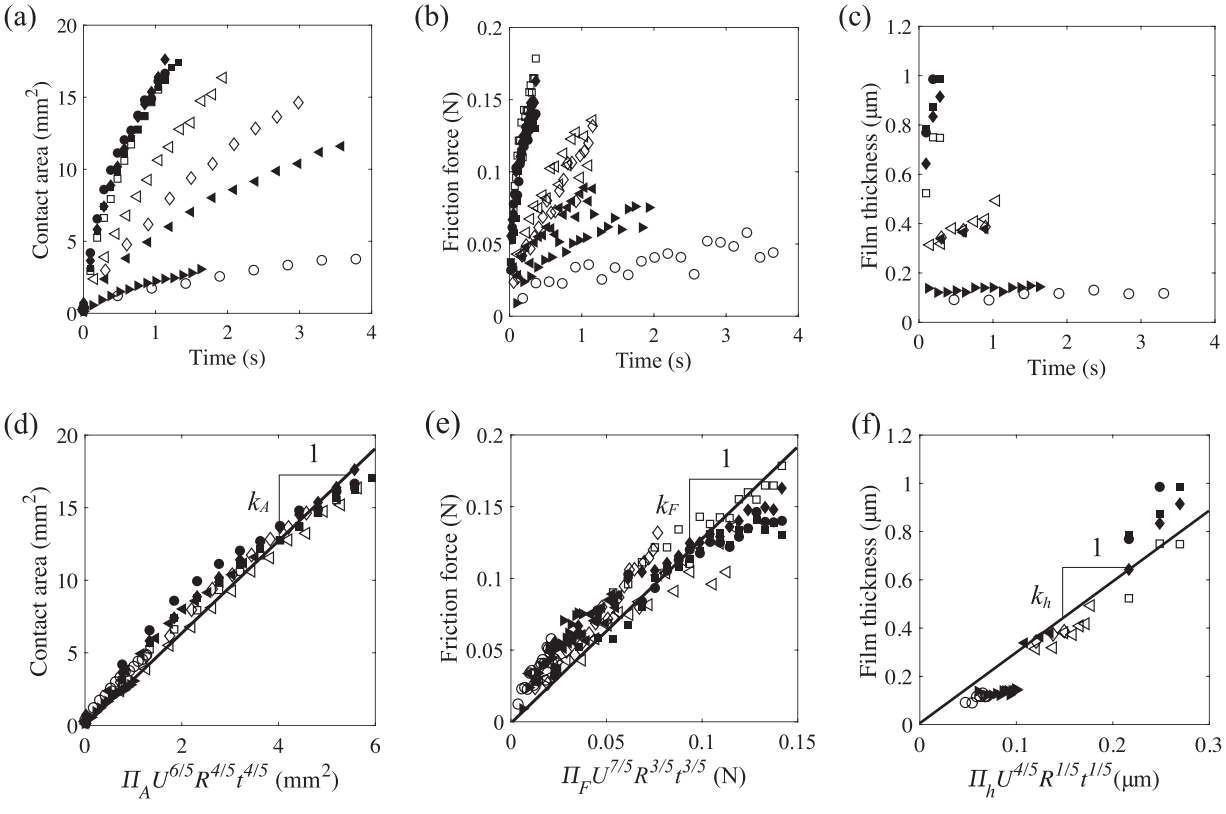

(g)

Symbol	U (m/s)	R (mm)	F_N (N)	Symbol	U (m/s)	R (mm)	F_N (N)
●	10	3	0.35	○	1	3	1.45
■	10	3	0.80	□	10	3	1.45
◆	10	3	1.78	◇	3.16	5	1.45
◀	3.16	3	1.45	◁	3.16	10	1.45
▶	1.89	3	1.45				

Fig. 4. (a) The contact area between the quartz plate and ice hemisphere versus time. (b) The friction force between the quartz plate and ice hemisphere versus time. (c) The film thickness deduced from the data of (a) and (b) in representative cases. (d) The contact area plotted according to scaling law (4) with $\Pi_A = \rho_w^{2/5}\rho_i^{-4/5}\mu^{2/5}L^{-2/5}$. The slope of the best fitting line, k_A, is 3.21 and the coefficient of determination, r^2, is 0.96. (e) The friction force plotted according to scaling law (7) with $\Pi_F = \rho_w^{4/5}\rho_i^{-3/5}\mu^{4/5}L^{1/5}$. The slope of the best fitting line, k_F, is 1.22 and the coefficient of determination, r^2, is 0.79. (f) The film thickness plotted according to scaling law (6) with $\Pi_h = \rho_w^{-2/5}\rho_i^{-1/5}\mu^{3/5}L^{-3/5}$. The slope of the best fitting line, k_h, is 2.93 and the coefficient of determination, r^2, is 0.86. (g) The legend and experimental conditions that are linked to the data of (a)–(f).

shows the computed value of h from measured values of A and F versus time, which were used to plot h according to our scaling law (6) in Fig. 4(f). We find two salient features of the behavior of water film thickness. First, time-dependence of the water film thickness is very weak for increasing like $t^{1/5}$, as predicted by Eq. (6). Second, the thickness varies from 0.1 to 1 μ m in our experimental conditions. The result is reasonable considering that the previously measured values of water film thickness in the sliding test of ice are approximately 0.4 μ m for $U \in (0.01 - 0.1)$ m s^{-1} [37] and $5 - 10$ μ m for $U \sim 17$ m s^{-1} [38]. The theoretically predicted friction coefficients, F/F_n with F_n being the normal load, for the sliding speeds similar to ours [6,20], $U \in (1 - 10)$ m s^{-1}, range from 10^{-3} to 10^{-1}, which are consistent with our measurement results of $0.005 - 0.4$. Therefore, the melted film of the order of 100 nm thickness with no significant temporal change arises when a solid plate slides on hemispherical asperities of ice in our experimental conditions.

In the hydrodynamic regime, the friction force is in general dependent on the normal load, F_n, as well as the sliding velocity and the viscosity of liquid film [6,22,23]. However, we see that the scaling law for the friction force (7) is independent of F_n. Also, our experimental measurements in Fig. 4(d) show that the friction force increases by less than 30% as the normal load increases by 10 folds from 0.35 N to 1.78 N for $U = 10$ m s^{-1} and $R = 3$ mm. Such insensitiveness to the normal load is reflected in our model where the squeezing flow rate, $\dot{\Omega}_s$, is ignored as compared with the ice melting rate, $\dot{\Omega}_m$, and liquid outflux due to plate translation, $\dot{\Omega}_t$. When the effects of $\dot{\Omega}_s$ on the film thickness is no longer negligible, the friction force should be dependent on the normal load, which was indeed observed in the previous studies [6,37] using a significantly higher pressure (~ 1 MPa) than our experiments ($\sim 10^{-2}$ to 10^{-1} MPa).

3.2. Extension to general flat ice surfaces

Upon the basis of the dependence of friction force on the relevant experimental parameters as we have found in Eq. (7), we can predict the friction force between smooth solid and ice plates with

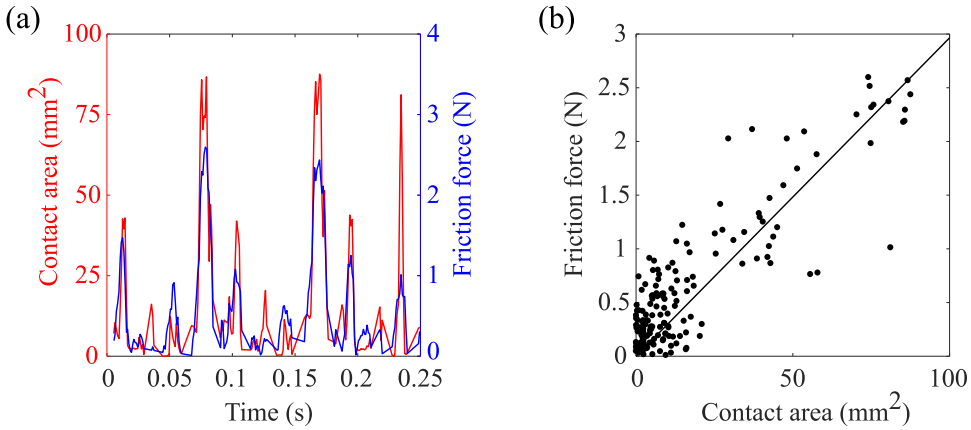

Fig. 5. (a) The simultaneously measured data of the real contact area and the friction force. The experimental conditions are such that $T = -0.5$°C, $U = 10$ m s^{-1}, and $F_n = 1.2$ N. (b) The friction force versus contact area, which allows us to find the average film thickness from the slope of the best fitting straight line. The coefficient of determination, r^2, is 0.72.

hemispherical bumps, which may serve as a simple model for general rough surfaces rubbing against each other. Because the effect of bump geometry, R, on the friction force is known, we compare the friction forces of two surfaces with identical contact area. The ratio of the contact area to the entire surface area is referred to as the bearing ratio [10], whose dependence on the removed surface thickness (H in our notation) has been assumed to play an important role in determining the ice friction. For $A \approx 2\pi RH$, if ice surface 1 has n_1 hemispherical bumps with radius of curvature R_1, ice surface 2 must have $n_2 = (R_1/R_2)n_1$ hemispherical bumps with radius of curvature R_2 in order for the two different ice surfaces to have the same bearing ratio through entire H. If the bumps of surface 2 have $R_2 = 10R_1$, their number should be $n_2 = n_1/10$, which gives the friction force $F_2 = (R_1/R_2)^{2/5}F_1 = 0.4F_1$ from Eq. (7). This indicates that the surfaces of identical bearing ratio through entire bump height experience different friction forces if the bump sizes are different. That is, the surfaces with greater bumps (e.g. surface 2) experience lower friction force than the surfaces with the same bearing ratio but smaller bumps (e.g. surface 1).

The real contact areas of an ice plate with a flat face of quartz prism are shown in Fig. 2(b). A remarkable feature we find, for the duration (2.5 ms) while any arbitrary point in ice appearing at the right side of a viewing window travels to the left side, is that the tails behind dark spots elongate with time. As the contact spot moves with the ice at U, the liquid film dragged with the spot has the average velocity of $U/2$ if the Couette flow arises as we assume in our model. We indeed see that the tail grows at approximately 5 m s^{-1} while the slider moves at 10 m s^{-1}, supporting our assumption of flow field in the liquid film.

The high-speed imaging results of the real contact area of flat surfaces of ice and quartz allow us to plot the temporal evolution of the contact area with time in Fig. 5(a), where the measured data of friction force, F, are plotted together. It is evident that the contact area and friction force are strongly correlated. Since the friction force due to viscous shear is given by $F = (\mu U/\tilde{h})A$, we find the average film thickness $\tilde{h}$ by plotting F versus A as shown in Fig. 5(b). The slope of the best fitting straight line finds $\tilde{h}$ to be 603 nm. This value lies within the range of what has been obtained from the hemispherical ice experiments and from previously reported measurements [37]. Although the duration of contact is relatively short and the bump size is unknown *a priori* in the flat specimen test, our model, Eq. (6), has allowed us to estimate the thickness of liquid film in the general flat ice surfaces from the results of hemispherical ice specimens thanks to weak dependency of the liquid film thickness on t and R: $h \sim R^{1/5}t^{1/5}$.

4. Conclusions

We have investigated the temporal evolutions of the friction behavior between ice and a solid slider using novel experimental techniques and theoretical analysis. We have utilized the optical principle of total internal reflection to visualize their real contact area in situ. Ice hemispheres have been adopted as a model of individual ice asperities sliding against a flat surface. By balancing the frictional heat generation rate with the heat consumption rate for melting, we have obtained scaling laws of the contact area, liquid film thickness and friction force as a function of the sliding velocity, radius of curvature and time as well as the material properties. The experiments with flat ice surfaces have visualized the temporal evolution of the real contact area between ice and a high-speed slider. It has been shown that the instantaneous friction force and the contact area are strongly correlated, allowing us to estimate the liquid film thickness from the theoretical model developed for the ice hemisphere upon the basis of weak dependence of film thickness on the bump size and time.

Although the effects of the normal load and temperature on the friction behavior are insignificant owing to the negligible squeezing rates of the liquid film and conduction heat transfer, respectively, the friction behavior of ice asperities in wider range of experimental conditions awaits further investigation for more general understanding of ice friction. Using our experimental techniques to observe the real contact area of flat ice surface and slider in situ, various physical phenomena can be investigated including the emergence of contact spots, evolution of liquid tails due to film dragging, capillary trapping of liquid at the edges of the specimens. While we inferred the film thickness from the simultaneously measured data of contact area and friction force in this work, the thickness can be directly obtained through the capacitance measurement [38]. Moreover, the spatial variation of the liquid film thickness obtained via interferometry [39] can provide rich information of the ice melting process due to high-speed sliding.

Our theoretical framework and experimental techniques to investigate how friction arises when the rubbing materials are melted in the contact spots can be applied to a variety of practical and natural situations in addition to ice friction. Failures of mechanical elements like shafts, bearings and pistons often involve melting of the rubbing surfaces due to inadequate function of lubricants. Frictional melting is a key process responsible for the rock failure and fault slips in geology and seismology [40]. Moreover, complicated friction phenomena associated with melting of vis-

coelastic polymeric materials and porous materials like snow, natural ice, and rocks are to be considered in the future to further our understanding of the dynamic friction processes in realistic settings.

Declaration of Competing Interest

The authors declare that they have no known competing financial interests or personal relationships that could have appeared to influence the work reported in this paper.

CRediT authorship contribution statement

Changho Yun: Methodology, Investigation. **Jin Woo Choi:** Formal analysis. **Hyungseok Kim:** Validation, Writing - original draft. **Dongjo Kim:** Investigation. **Ho-Young Kim:** Conceptualization, Writing - original draft, Supervision.

Acknowledgments

This work was supported by National Research Foundation of Korea (Grant no. 2018052541) via SNU-IAMD.

Supplementary material

Supplementary material associated with this article can be found, in the online version, at doi:10.1016/j.ijheatmasstransfer.2020.120166

References

[1] M. Faraday, Experimental Researches in Chemistry and Physics, Taylor and Francis, London, 1859.
[2] J. Joly, The phenomena of skating and prof. j. thomson's thermodynamic relation, Sci. Proc. R. Soc. Dublin New Ser. 5 (1886) 453.
[3] F.P. Bowden, Friction on snow and ice, Proc. R. Soc. Lond. A 217 (1953) 462–478.
[4] R. Rosenberg, Why is ice slippery? Phys. Today 58 (2005) 12.
[5] F.P. Bowden, T.P. Hughes, The mechanism of sliding on ice and snow, Proc. R. Soc. Lond. A 172 (1939) 280.
[6] L. Bäurle, D. Szabó, M. Fauve, H. Rhyner, N.D. Spencer, Sliding friction of polyethylene on ice: tribometer measurements, Tribol. Lett. 24 (2006) 77–84.
[7] G. Sazaki, S. Zepedaa, S. Nakatsuboa, M. Yokominec, Y. Furukawa, Quasi-liquid layers on ice crystal surfaces are made up of two different phases, Proc. Natl. Acad. Sci. USA 209 (2012) 1052–1055.
[8] D.C.B. Evans, J.F. Nye, K.J. Cheeseman, Kinetic friction of ice, Proc. R. Soc. Lond. A 347 (1976) 493.
[9] A.D. Roberts, J.C. Richardson, Interface study of rubber-ice friction, Wear 67 (1981) 55–69.
[10] L. Bäurle, T.U. Kaempfer, D. Szabó, N.D. Spencer, Sliding friction of polyethylene on snow and ice: contact area and modeling, Cold Reg. Sci. Technol. 47 (2007) 276–289.
[11] D.D. Higgins, B.A. Marmo, C.E. Jeffree, V. Koutsos, J.R. Blackford, Morphology of ice wear from rubber-ice friction tests and its dependence on temperature and sliding velocity, Wear 265 (2008) 634–644.
[12] T. Fülöp, A.J. Tuononen, Evolution of ice surface under a sliding rubber block, Wear 307 (2013) 52–59.
[13] A.J. Tuononen, A. Kriston, B. Persson, Multiscale physics of rubber-ice friction, J. Chem. Phys. 145 (2016) 114703.
[14] S. Hemette, J. Cayer-Barrioz, D. Mazuyer, Friction setup and real-time insights of the contact under controlled cold environment: the KŌRI tribometer for rubber-ice contact application, Rev. Sci. Instrum. 89 (2018) 123903.
[15] T. Komiyama, T. Iwai, Y. Shoukaku, Effect of the pores in porous rubber on water flow at the contact area, Tire Sci. Technol. 44 (2016) 22–35.
[16] Y. Minami, T. Iwai, Y. Shoukaku, Observation of water behavior in the contact area between porous rubber and a mating surface during sliding, Tire Sci. Technol. 40 (2012) 186–200.
[17] L.G. Gitzendanner, Optical observations of sealing phenomenon, in: Proceedings of the Conference on Design of Leak-tight Separable fluid Connectors, 1964, pp. 327–344.
[18] S.M. Benabdallah, J. Lapierre, A new device for measuring the real area of contact of polymeric material by the perturbation of total internal reflection, J. Mater. Sci. 25 (1990) 3497–3500.
[19] I.V. Kragelsky, N.B. Demkin, Contact area of rough surfaces, Wear 3 (1960) 170–187.
[20] L. Makkonen, M. Tikanmäki, Modeling the friction of ice, Cold Reg. Sci. Technol. 102 (2014) 84–93.
[21] A.J. Fowler, A. Bejan, Contact melting during sliding on ice, Int. J. Heat Mass Transf. 36 (1993) 1171–1179.
[22] P. Oksanen, J. Keinonen, The mechanism of friction of ice, Wear 78 (1982) 315–324.
[23] A.-M. Kietzig, S.G. Hatzikiriakos, P. Englezos, Physics of ice friction, J. Appl. Phys. 107 (2010) 081101.
[24] J.R. Blackford, G. Skouvaklis, M. Purser, V. Koutsos, Friction on ice: stick and slip, Faraday Discuss. 156 (2012) 243–254.
[25] S.C. Colbeck, A review of the friction of snow skis, J. Sports Sci. 12 (1994) 285–295.
[26] Y. Lyu, E. Bergseth, U. Olofsson, Open system tribology and influence of weather condition, Sci. Rep. 6 (2016) 1–11.
[27] F.E. Kennedy, E.M. Schulson, D.E. Jones, The friction of ice on ice at low sliding velocities, Philos. Mag. A 80 (2000) 1093–1110.
[28] J. Heierli, P. Gumbsch, M. Zaiser, Anticrack nucleation as triggering mechanism for snow slab avalanches, Science 321 (2008) 240–243.
[29] B. Slater, A. Michaelides, Surface premelting of water ice, Nat. Rev. Chem. 3 (2019) 172–188.
[30] D. Limmer, Closer look at the surface of ice, Proc. Natl. Acad. Sci. 113 (2016) 12347–12349.
[31] M.P. Goertz, X.-Y. Zhu, J.E. Houston, Exploring the liquid-like layer on the ice surface, Langmuir 25 (2009) 6905–6908.
[32] A. Döppenschmidt, H.J. Butt, Measuring the thickness of the liquid-like layer on ice surfaces with atomic force microscopy, Langmuir 16 (2000) 6709–6714.
[33] K. Murata, H. Asakawa, K. Nagashima, Y. Furukawa, G. Sazaki, In situ determination of surface tension-to-shear viscosity ratio for quasiliquid layers on ice crystal surfaces, Phys. Rev. Lett. 115 (2015) 256103.
[34] J.F.D. Liljeblad, I. Furó, E.C. Tyrode, The premolten layer of ice next to a hydrophilic solid surface: correlating adhesion with molecular properties, Phys. Chem. Chem. Phys. 19 (2017) 305–317.
[35] P.G. de Gennes, Wetting: statics and dynamics, Rev. Mod. Phys. 57 (1985) 827–863.
[36] H.-Y. Kim, H.J. Lee, B.H. Kang, Sliding of liquid drops down an inclined solid surface, J. Colloid. Interface Sci. 247 (2002) 372–380.
[37] L. Canale, J. Comtet, A. Niguès, C. Cohen, C. Clanet, A. Siria, L. Bocquet, Nanorheology of interfacial water during ice gliding, Phys. Rev. X 9 (2019) 041025.
[38] W. Ambach, B. Mayr, Ski gliding and water film, Cold Reg. Sci. Technol. 5 (1981) 59–65.
[39] R. Gohar, A. Cameron, Optical measurement of oil film thickness under elasto-hydrodynamic lubrication, Nature 200 (1963) 458–459.
[40] G.D. Toro, R. Han, T. Hirose, N. De Paola, S. Nielsen, K. Mizoguchi, F. Ferri, M. Cocco, T. Shimamoto, Fault lubrication during earthquakes, Nature 471 (2011) 494–498.